A Wireless Head-mountable Device with Tapered Optical Fiber-coupled Laser Diode for Light Delivery in Deep Brain Regions

Mohamed S. Emara, *Member, IEEE*, Marco Pisanello, Leonardo Sileo, Massimo De Vittorio and Ferruccio Pisanello

Abstract— **Optogenetics sets new experimental paradigms that can reveal cell type-specific contributions on the neural basis of behavior. Since most of the available systems for this purpose are based on approaches that tether animals to a set of cables, recent research activities have been focused on minimizing external factors that can alter animal movements. Current wireless optogenetic systems are based on waveguide-coupled LED and implanted µLEDs. However, each configuration separately suffers from significant limitations, such as low coupling efficiency, penetration depth and invasiveness of waveguide-coupled LED, and local heat generated by implanted µLEDs. This work presents a novel wireless head-mountable stimulating system for a wide-volume light delivery. The device couples the output of a semiconductor laser diode (LD) to a tapered optical fiber (TF) on a wireless platform. The LD-TF coupling was engineered by setting up far-field analysis, which allows a full exploitation of mode division demultiplexing properties of TFs. The output delivered light along the tapered segment is capable of stimulating structures of depths up to ~2mm. TFs are tapered to a gradual taper angle ($\Psi\sim2°$ to $\Psi\sim10°$) that ends with a sharp tip (~500 nm) for smooth insertion and less invasiveness. Thus, the proposed system extends the capabilities of wireless optogenetic by offering a novel solution for wide volume light delivery in deep brain regions.**

*Index Terms—***Deep brain stimulation, optogenetics, tapered optical fiber, semiconductor laser diode, wireless device.**

Mohamed S. Emara and Massimo De Vittorio are with Istituto Italiano di Tecnologia (IIT), Center for Bio-Molecular Nanotechnologies, Via Barsanti snc, 73010 Arnesano (LE), Italy, and Dipartimento di Ingegneria dell'Innovazione, Università del Salento, Via per Monteroni, 7300 Lecce, Italy (email: mohamed.emara@iit.it, massimo.devittorio@iit.it. Marco Pisanello, Leonardo Sileo and Ferruccio Pisanello are with Istituto Italiano di Tecnologia (IIT), Center for Biomolecular Nanotechnologies, Via Barsanti snc, 73010 Arnesano (LE), Italy (email: ferruccio.pisanello@iit.it).

I. INTRODUCTION

THE development of optogenetics [1] has offered neuroscientists a set of new tools to control neural activity by using visible light radiation. By genetic expression of light-gated ion channels and pumps, such as Channelrhodopsin2 (ChR2) and Halorhodopsin (Halo) [2], it is possible to stimulate or inhibit the generation of action potentials with high spatiotemporal resolution and cell-type specificity [3-5]. Since its first application in mammalian neurons [6], it has been clear that tissue absorption and scattering strongly influence (and limit) the spatial extension of light patterns that are used to trigger the electrical activity of neural cells [7]. For this reason, intense technology development has been devoted to improving light delivery into brain tissue [2, 8-10] by developing implantable micro light-emitting diodes (µLED) [11-18], silicon nitride or silicon dioxide waveguides [19, 20] and new generations of both polymeric and glass-based optical fibers [21-28]. However, most of these approaches tether the animal with electrical or optical connections to bench-top equipment, whereas most *in vivo* readout behavior experiments require to preserve the natural movements of the animal. Therefore, particular attention has been driven by the need of implementing wireless optogenetics stimulation with no (or very limited) constraints on animal movements.

The resulting wireless optogenetics stimulation technologies have adopted two main configurations: (i) fully-implantable devices that are based on LEDs and µLEDs [29-34], and (ii) head-mountable devices, which mainly adopt one of the following configurations: LEDs [35-38], µLEDs [12, 15, 39-43], waveguide-coupled LED [28, 44-49] or waveguide-coupled µLED [50-52]. Both approaches depend exclusively on LEDs, although they suffer from significant limitations. The broad emission of LEDs [11] leads to a low coupling efficiency to optical waveguides [53], resulting in a small illuminated volume and consequently in a low number of stimulated cells. The low coupling efficiency of LEDs is commonly compensated by a relatively large-diameter waveguide, which increases the invasiveness of the implant. As an alternative to large-core fibers, the emission power of LEDs can be increased to overtake the activation threshold of excitatory and inhibitory opsins (~1 mW/mm^2 and ~7 mW/mm^2, respectively) [54, 55] over wider volumes. However, this choice for a wireless solution is critical, since the level of power consumption would increase, leading to employing batteries with higher capacity or limiting the running time. On the other side, µLEDs are less invasive and can be implanted into deep brain areas such as the ventral tegmental area (VTA) [29], but when they are operated for long periods or at high powers to increase the stimulated volume, unavoidably increase local temperature of tissues [11, 15, 56], which may lead to thermal artefacts and increasing the damaging rate to in-contact tissues [54, 57].

The approach we report here is designed specifically for targeting deep brain regions in freely-moving animals; it overcomes the light delivery limitation of LEDs on wireless platforms, by coupling the output of a semiconductor laser diode to low invasive tapered fibers (TF). By implementing far-field analysis, LD-TF coupler was engineered to exploit the mode-division demultiplexing properties of TFs to generate a gradual outcoupling of guided modes along the taper. The light

emission length along the tapered segment can be tailored from ~400µm to ~3mm by acting on the taper angle (2°<Ψ<10°). This light emission length allows to stimulate the entire depth of functional structures in the mouse brain, such as the cerebral cortex, striatum and hippocampus. Our TFs were tapered to a sharp tip (~500 nm) for smooth insertion and less invasiveness, compared to previous systems (**Fig1 (a)**). The head-mountable device is powered by light-weight rechargeable batteries and triggered wirelessly for real-time control of neural activity by infrared (IR). Its light delivery capabilities, output optical properties, weight, size, and thermal behavior let us envision that this approach can represent an important complement to the currently available wireless systems for optogenetic stimulation.

II. SYSTEM DESIGN

The complete wireless optogenetic stimulation system consists of two modules: the TTL wireless transmitter, and head-mountable device, which receives the TTL signal and optically stimulate the brain tissues through the implanted TF. **Fig1 (b) and (c)** show the experimental model and block diagram of the proposed approach, respectively. The transmitter itself comprises a generator of a TTL trigger signal, which is subsequently transmitted by a single or group of IR LEDs (SFH4725S, OSRAM λ~950, emission angle 45°) to cover large and complex experimental environments. As shown in **Fig1 (b),** the head-mountable device at angle 0° with the emitter, can detect the signal successfully at a distance of ~60 cm from the emitter. A distribution of three IR LEDs is enough to cover a square area of ~0.3 m^2 from a height of ~60 cm, or a square area of 1.5 m^2 from a height of ~30 cm. **Fig1 (c)** exhibits the flow of the signal from the transmitter until it reaches the implantable fiber on the head-mountable device. The head-mountable device (15 x 13 x 15 (h) mm; 3.8 g) is divided into the headstage (3.3 g with batteries) and the implantable unit (0.5 g), which comprises the TF-coupled semiconductor LD. The implantable unit is attachable and detachable to and from the headstage by 2-pin receptacles.

The head-mountable device was designed to exploit the peculiar properties of TFs to obtain a wide volume light delivery with minimal invasiveness. To the best of our knowledge, all the waveguide-coupled wireless solutions in literature are based on LED and μLED [28, 44, 46-48, 50, 58]. In our case, TFs require a precise control over the modal content injected into the fiber since their working principle is based on the gradual leakage of guided modes along the taper [22]. This can hardly be achieved by using LEDs, which are well-known of their low coupling efficiency with waveguides, and wide irradiated angles due to the Lambertian emission pattern (from ~90° to 120°) [54, 59]. Laser Diodes (LDs) offers a more directional output. Here, the light injection system is based on OSRAM LD Q65111A0518, emitting at λ~450 nm, with minimum and maximum divergence angles $\theta_\perp$ x $\theta_{//}$: 4°x 18° and 25°x11°, respectively [60], which are matching well with the ~23° acceptance angle of 0.39 NA core/cladding 200/225 μm optical fibers.

The use of LDs instead of LEDs introduces some constraints on the design of a lightweight device. The LD must be supplied by a stable forward current (from anode to cathode)

to avoid fluctuations in the LD output optical power. Furthermore, it is well-known that LD surface temperature increases during the operation and it needs to be stabilized at almost room temperature for assuring a constant light delivery power during on pulses.

The headstage was designed to emit pulses of light on sub-milliseconds. This was obtained by designing the headstage to use a low number of components, connected in series, to minimize the latency with respect to the received TTL signal. The rising and falling times of the emitted pulses by the headstage is less than < 20 µs. **Fig1 (d)** shows the emitted light pulses by the head-mountable device at TTL trigger signal of 200 Hz and 10% duty cycle (D) with a resulting pulse width of 500 μs.

These design motivations and considerations lead to a headstage consisting of a stimulation module (**Fig2 (a)**) and a power module (**Fig2 (b)**). The stimulation module is centered on a spike-free switching LD-switch (IC-HKB MSOP8-TP, iC-Haus; 155 MHz; 1.5 ns forward current rise and fall time). It switches the LD on and off wirelessly, according to the received signal by the IR phototransistor (TEKT5400S-ASZ, Vishay; 37°). The output optical power of the LD is regulated by a surface mount 10k Ω trimmer, which regulates the voltage on the "CI" pin of the LD switch. The applied voltage to the "CI" pin sets the fed forward current to the LD. The Schottky and Zener diodes are in parallel with the LD to protect it against reverse polarity connection, electrostatic discharge and overrated forward voltages. The surface temperature of the laser diode was stabilized by adding a heatsink. The system is powered by two 3.7 V/ 50 mAh lithium rechargeable batteries. The input voltage 6V goes directly to the LD and dual-voltage regulator (**Fig2 (b)**). The dual-voltage regulator (ON Semiconductor, NCP5504DTRKG) regulates the input voltage to 5V (the LD switch), and 3.3V (the trimmer). The Diode D1 (Bourns, CD0603-B0230) in parallel with the battery terminals protects the circuit against reverse polarity connection. The platform that electrically connects all the components and holds them mechanically is a thin 0.3 mm double-sided flexible PCB 14.0 mm x 13.5 mm (**Fig2 (c-d)**). The flexible and thin PCB contributes to minimizing the headstage total weight (0.8 g after hand soldering all the components, without batteries).

III. COUPLING TAPERED OPTICAL FIBER FOR WIDE VOLUME LIGHT DELIVERY

Towards minimizing the size of the implantable unit, a butt-coupling between the TF and LD has been realized, as sketched in **Fig3 (a)**. Considering the minimum ~1.02 mm distance between the LD emission point and the TF input facet, LD emission is projected on a ~0.07 mm^2 elliptic surface, which overfills the ~0.03 mm^2 surface area of the fiber core (see launch conditions between the laser beam and fiber core in **Fig3 (a)**). The result of the LD beam divergence matches well with the 23° acceptance angle of 0.39 NA and $\emptyset$200 μm core fiber. This is an important aspect, since TFs emission properties are mostly based on the modal content of light guided into the fiber, which are strongly dependent on the input angle of light injected into the fiber. As already demonstrated in refs [21, 22, 25], injecting rays into the fiber facet with low input angles (low transversal component of the wave-vector K_t) results in out-

coupled rays closer to the fiber tip, whereas injecting rays with higher input angles (high K_t modes) leads to out-coupling further from the taper tip (see ray tracing schematics in **Fig3 (b)**). Therefore, to get the longest possible light emission length over the taper segment, the system must inject light into the TF with the highest possible angular range while preserving a high-enough coupling efficiency at the same time.

To verify that the butt-coupling method allows injecting guided modes with a wide-enough range of K_t values, the far field system depicted in **Fig4 (a)** was used. A patch fiber was butt-coupled to the LD TO38 package, while the fiber output was detected by Lens L1 (focal length, f1=4.6 mm), generating a far field pattern of the light emitted by the optical fiber in its focal plane. Such pattern was then magnified by a factor ~3.3 and imaged over a sCMOS camera by lenses L2 (f2=30 mm) and L3 (f3=100 mm). In the resulting far-field images, K_t is decomposed along the two-orthogonal-axis of the sensor chip in two components, namely K_x and K_y. In particular, K_t is related to the signal detected by the sensor chip at distance r from its center by the following equation:

$$r = \frac{F1\ F3}{F2} \tan\left(\sin^{-1}\left(\frac{\lambda}{2\pi} K_t\right)\right)$$

Typical far-field patterns for different relative TF-LD positions are shown in **Fig4 (b)**, with the correspondent decomposition on the K_x axis and total emitted power ($P_{Coupling}$) displayed in **Fig4 (c-d)**, respectively. For evaluating the achieved coupling position in respect to the outcoupled light emission length along the taper (L), we collected fluorescence images, obtained by submerging a TF with Ψ~4° into a droplet of PBS:fluorescein (see **Fig5 (a)**). The coupling position #4 shows the widest K_t interval and the longest emission from the taper (L~1.48 mm). This result is almost equal to the maximum emission length L~1.66 mm that was achieved by bench-top laser for the same TF. On the contrary, for coupling position #5 (highest coupling efficiency) L~0.66 mm was obtained, due the narrower set of K_t values injected into the waveguide. The repeatability of the coupling position was estimated by running multiple alignment sessions. On a total of n=3 independent sessions, a standard deviation of σ_L ~0.10 mm over an average emission length of L~1.34 mm was reported.

Total emitted power by the TF was tested by setting LD emitting power at P_{LD}~16 mW. Position #4 results in a lower coupling efficiency (~25%) in comparison with position #5 (~44%) (**Fig4 (d)**). However, the power density generated by the taper at coupling position #4 is ~ 10 mW/mm^2, which is well above the ~1 mW/mm^2 for activating ChR2 [6]. The related spatial distribution (P) is shown in **Fig5 (b)** for a TF at the coupling position #4. P was calculated by a Matlab script that integrates the density profile over the tapered surface for a given total output power. The calculations were done under the assumption of rotational symmetry around the taper axis, and considering the proportionality between the grayscale values registered by the sCMOS sensor and P (more details on these calculations are given in the Appendix).

As further validation that this method allows obtaining a functional coupling between TF and LD, and that it preserves the basic operational features of TFs [25], we tested TFs with

taper angles ranging from Ψ~2° to Ψ~10°. As shown by the data displayed in **Fig5 (c)**, the emission length (L) can be tailored from a few hundred of micrometres to ~3 mm by modifying the taper angle at the same coupling position #4 for each case. The output power distribution for a TF with a very low Ψ is also shown in the Appendix (**Fig.S2**).

IV. TIME STABILITY OF LASER DIODE EMISSION

It is well known that the stability of the output optical power (P_{LD}) of a semiconductor LD can be affected by a noisy forward current or by non-efficient heat dissipation, which lowers the LD forward voltage and directly decreases the emitted power. This phenomenon is shown in **Fig6 (a)**, the T038 LD (without a heatsink) is supplied with a stable forward-current, according to TTL trigger signal with frequency/duty-cycle 100mHz/50% at P_{LD}~20mW. This signal was chosen as a "heavy load case reference", since it sets the LD 5s-on and 5s-off, while most optogenetics stimulation protocols are on the tens of milliseconds range with small duty cycles [8]. For ~3 minutes of constant stimulation, the LD generated 22 5s-pulses; the LD surface temperature (T_{LD}) reached 48° C at the end of this operational cycle. Due to this rapid increase of the LD surface temperature, the P_{LD} decayed ~ 50%. To examine this phenomenon, we measured power losses (PL%) for different P_{LD} settings for the same TTL trigger signal (100mHz/50%/22-pulses). As shown in **Fig6 (b)**, low levels of P_{LD} induce a higher power decay, since the temperature increase can induce subthreshold operation as illustrated in the datasheet [60]. For further examination of the thermal behavior of the LD, in **Fig6 (c-d)** we recorded the surface temperature of the LD (T_{LD}) package and the PL% at two different power levels P_{LD}~20 mW and P_{LD}~40 mW along 5 different stimulation protocols commonly used for *in vivo* stimulation [15, 31, 61-63] (details of the protocols are given in the caption of **Fig6**). This feature prevents using the LD without the addition of a heatsink.

We worked on stabilizing the P_{LD} by increasing the heat-dissipating surface, and therefore stabilize the power level and surface temperature. We fixed an aluminium ring on the base of the LD package (**Fig6 (e2)**), and we used a metallic ferrule for connectorizing the TF (**Fig6 (e3)**). All components were secured by the thermal epoxy (TBS20S, Electrolube) for better heat dissipation (**Fig6 (e4)**). Those added parts increased the surface area of the LD package by three times, subsequently, the heat dissipation enhanced as shown in **Fig6 (f, g, h, i)** in respect to the collected data of the bare LD in **Fig6 (a, b, c, d)**. For the 100mHz/50%/22-pulses TTL protocol, for P_{LD}~20mW a power loss of ~9% was recorded (**Fig6 (f)**), which drops to ~0% for P_{LD}~40mW (**Fig6 (g)**). Similar improvements were obtained for the stimulation protocols used in refs [15, 31, 61-63] (**Fig6 (i)**), for which all tests at P_{LD}~40mW resulted in no power loss, while P_{LD}~20mW induces power losses well below 10% in all cases.

V. POWER CONSUMPTION

Typical power density used for *in vivo* optogenetic experiments ranges from 1 to 10 mW/mm^2 [8, 64]. **Fig7 (a)** shows the total current consumption of the head-mountable device at different applied voltages to the "CI" pin—the LD forward current control. At V_{CI}=1.58 V, the coupler output

optical power (P_{TF}) is 4 mW (e.g. intensity ~12.5 mW/mm^2 along a Ψ~4° TF), and the headstage total current consumption is 45 mA. The two main factors that control the total energy consumptions and therefore the battery running-time are the emitted P_{LD} and duty cycle of the stimulus TTL signal. **Fig7 (b)** shows the energy consumption at different optical power densities: at the end of 3 minutes of constant stimulation of pulses with a duty cycle of 50%, total energy consumption of ~25 J was registered.

Since the commonly used optogenetic stimulation protocols rely on short pulses [8, 35, 37], the maximum pulsed discharge current is an essential factor for setting the criteria for choosing the right powering batteries. Considering the power requirements of the head-mountable device, the system is supplied by two 3.7V/50mAh (5 x 12 x 15 mm) lithium polymer rechargeable batteries (GM051215, PowerStream) in series. These batteries are characterized by low weight (~1 g each), reasonable capacity (~4 hours of continuous operation at D 25% & pulse intensity of ~ 10 mW/mm^2), and a high discharge current, 1C (discharge rate). **Fig7 (c)** shows the emitted optical power of the head-mountable device when it is operated continuously and without intervals at three typical optogenetic TTL trigger signals; the data were collected while the device was powered by the previously mentioned batteries. A slight decrease in the total output (~ <0.4 mW) at the end of the operational cycle along the three cases was observed due to the minor increase of the LD's temperature during the operation and discharging the battery at a load (45 mA) almost equal to the maximum discharging current (50 mA). Pictures of the whole device are shown in **Fig8**. The headstage total weight is 3.8 g (see **Table I**), and the dimensions are 15 x 13 x 15 (h) mm^3, including batteries.

VI. DISCUSSION

We present a wireless head-mountable device that exploits the optical properties of TFs to obtain wide-volume light delivery in freely-moving animals. The miniaturized device (15 x 13 x 15 (h) mm^3; 3.8 g with batteries) is triggered wirelessly by λ~950 nm infrared LED and powered by two rechargeable batteries in series. The head-mountable device consists of the headstage (composed by stimulation and power modules) and the implantable unit for light delivery. The light delivery is based on 0.39 NA TF ($\emptyset$200 µm core) coupled to a λ~450 nm semiconductor LD, a unique combination that achieves a wide-volume light delivery and reduced invasiveness. The fiber outer diameter (d= $\emptyset$225 μm) was tapered to ~500 nm tip that guarantees a smooth insertion into brain tissues and reduction of the implant cross-section to a sharp tip. The taper emission length can be tailored from ~400µm to ~3mm by changing the taper angle ($2° < \Psi < 10°$). The implanted TF is connectorized to a ferrule for a butt coupling with the LD. The length of the fiber that emerges out of the ferrule cannot be shorter than the taper length (l), with $l=d/(2*tan(\Psi/2))$. This is due to the fact that the glue used to fix the fiber into the ferrule would act as a "cladding", influencing modal configuration into the fiber and unavoidably modifying the light delivery properties of TFs. The metallic ferrule that is connectorized to the TF has mainly three functions: (i) the metallic surface of the ferrule, which is in a direct contact with

the laser diode cane partially participates with stabilizing the LD's surface temperature, (ii) the ferrule makes the handling of the tapered fiber for the alignment process easier and more secure, and (iii) ferrule length here works as a bend relief for a cable; it prevents the bending of the fiber near the coupling point, which would induce modal mixing. The system emits stimulation pulses with rising and falling time <20 μs with a complete control of the LD thermal behavior for TTL pulses up to 5s. The outcoupled power along the tapered segment can be controlled by both, manually by the 10k Ω trimmer or the transmitted duty cycle. This latter possibility will mostly depend on the time response of the used opsin. The main characteristics of the system have been summarized in **Table II**.

To the best of our knowledge, the proposed head-mountable device is the first to be specifically designed for wide-volume wireless light delivery, by exploiting the optical properties of TFs. LEDs and µLEDs are the first and only solution, so far, for coupling light into implantable waveguides on wireless platforms [28, 44-48]. However, LDs offers more directional optical output in comparison to LEDs, resulting in a better coupling efficiency with TFs and full exploitation of their mode division demultiplexing properties. By using optical far-field analysis, the butt coupling between the LD and TF was optimized for obtaining the longest possible emission along the taper, while preserving a high-enough power density for ChR2 stimulation (10 mW/mm^2). In the condition of the longest possible emission along the taper segment, the coupling efficiency was found to be 25%. Although this is not the maximum achievable coupling efficiency (which is 44%, see **Fig4 (d)**), it allows overtaking opsins stimulation thresholds and it is considerably higher than the typical coupling efficiency ~1% of LEDs with flat-cleaved fibers ($\emptyset$200 μm core) [7]. In the wireless CerebraLux system [46], for instance, the coupling efficiency of the LED-coupled to 0.63 NA flat optical fiber with double size core ($\emptyset$450 μm core) is only 10.2%.

Another important advantage with respect to LEDs, LDs are more efficient in energy conversion [65]. By employing two 3.7V/50mAh batteries (~1 g each), the headstage can generate power density levels up to ~10 mW/mm^2 (see **Fig5 (b)**) with full emission length that can be tailored from ~0.7 to 3.4 mm (see **Fig5 (c)**). In comparison with the operational time of other systems, the programmable LED stimulator presented in ref [37] is composed by a head-mountable device (2.4 g) powered by single 3.7V/10mAh battery (0.52 g) that can run the system for 67 minutes at TTL stimulation parameters (50 ms pulses at 10 Hz for 2 s duration at 5 s intervals), and at power intensity 6.07 mW/mm^2 with LED (1.6 x 0.8 x 0.68 mm). The running time of the that system can be increased to ~2 h by using a larger battery 20 mAh (1.39 g) that will increase the total mass of the head-mountable device to 3.27 g instead of 2.4 g. The system we propose in this work can emit pulses at the same TTL stimulation parameters with a 1.65x higher intensity (10 mW/mm^2) with a longer illuminated segment ~2mm and running time of ~7 h, in a comparable mass (3.27g $\approx$3.8 g). This means that the proposed system is fit to run optogenetics stimulation experiments for reasonable durations before the need to be recharged. The batteries can be

recharged on board, and by the connecting receptacles, the headstage is detachable from the implantable part.

A. In comparison with flat cleaved optical fibers-coupled LED

Waveguide-coupled LED is an interesting option for targeting deeper layers. The deep-brain stimulator presented in ref [48], for instance, is based on optical fiber-coupled LED. The system is powered by two solid-state batteries ($50\mu Ah$); by calculation, the batteries can run the system for one hour of continuous operation at 50% D and $27mW/mm^2$ of irradiance out of the fiber facet (current consumption 21.01 mA). On the other side, our system with a flat fiber can supply 44.5 mW/mm^2 (1.6x more) out of the fiber facet at almost the same current consumption level (25 mA) for four hours of continuous operation (4x more) at 50% D. As a further comparison, the head-mountable (4.9 g) device for optical stimulation (flat optical fiber-coupled (core: $\varnothing 200$ μm) LED) and neural recording proposed in ref [47], which is powered by a single 3.7V/100mAh battery (2.1 g, 70 minutes at 10% D, 150 mA stimulation current for 70 mW/mm^2 (2.19 mW)). If the same flat fiber (200 μm) is connected to our LD-based system the output power out of the fiber tip will be $225mW/mm^2$ (7 mW, 3.2x more) at total current consumption of 45 mA (6.7x less), and at 10% D the system can run continuously for ~10 h (8.5x more). Moreover, we are utilizing the photonic properties of TF, the illuminated area of the TF is larger than the illuminated area of the flat fiber [10, 21, 25]. Besides, the penetration depth of the TFs is deeper than the one of flat fibers so that high power transmission to overcome absorption and scattering factors can be avoided as described in our previous work [25]. This let us envision that our wireless device is more suitable for targeting deep brain regions than previous devices that are based on flat fiber-coupled LED [48], and can be considered as the second generation of wireless deep brain stimulation tools. The solution proposed here brought the capabilities of TF wide-volume light delivery on a self-consistent wireless platform that is comparable in size and weight with the other systems (see the comparison in **Table III**).

B. In comparison with μLEDs shank

μLEDs shanks are another strong alternative for light delivery that has been utilized on a wireless platform [15, 32, 33, 39-41, 66]. It is a versatile option that can be presented in different topologies with low Young's modulus for matching the mechanical properties of brain tissues. The number of μLEDs on the implantable shank can be increased or decreased according to the design with the desired pitch. To our knowledge, the presented μLED shanks on wireless platforms carry from 1 to 4 μLEDs for localized light delivery with overall shank width of 250-500 μm and maximum full emission length not longer than ~880 μm, by activating all the emitters simultaneously (see the comparison in **Table IV**). Beside the complexity of fabrication, the main challenge that implanted μLEDs shanks face is the management of the thermal behaviour. Electronics in direct contact with tissues increase the local temperature, in particular when long stimulation pulses are needed [11, 15, 56]. Even 1-2° C temperature increase may cause tissue lesioning and adverse behavior [11, 57, 67, 68]. In our case here, TFs avoid the direct contact of electronics with

tissues, reduce the invasiveness factor in comparison with other approaches by tapering the outer diameter ($\varnothing 225$) of optical fibers to a sharp tip ~500 nm (see probe thickness and width on **Table IV**, and **Table V**), and have a longer light emission length ~2 mm around 360° (see **Fig5 (c)** and **Table IV**). μLED shanks in wireless applications are designed for localized light delivery, that is directly reflected in small illuminated volumes and directly a lower power demand than wide-volume light delivery systems (the proposal of this work). Consequently, μLED shanks can be powered by RF scavenging solutions, which contributes mainly in miniaturizing the total size, or by small batteries with low capacity(8 mAh) [39].

C. Wireless optogenetic powering methods

Powering methods for wireless and wearable applications, in general, is nearly among the most challenging aspects that face implantable free movement devices. We have summarized the main powering methods and wireless data transfer approaches for wireless optogenetic devices as well as for electrophysiological neural stimulation and recording in **Table V**: photovoltaics [41], wireless power transfer (WPT) [15, 29-34, 36, 44, 49, 50, 69], and batteries [28, 37-40, 45-47, 58, 70, 71]. WPT [72] is an inevitable approach for fully-implantable systems [29-34], which can be covered by a polydimethylsiloxane (PDMS) layer for full immersion. When WPT is applied to head-mountable devices, it is often accompanied by a supercapacitor for buffering, energy storage and stable powering [15, 36, 44, 50, 69]. WPT works on miniaturizing the implant whether it is near field magnetic resonant coupling (1-2 MHz to 13.56 MHz) [73] or far-field energy transfer (420 MHz to 2.4 GHz) [74, 75]. For example, the wireless optofluidic system (15 x 15 x 7 mm^3) weights ~1.8 g when powered by batteries [39]; the size and weight of the system goes significantly down until 125 mm^3 and 220 mg once the system is powered by RF complex antenna setup [33]. However, the operational distance gets down to 10 cm instead of 3 m previously. This is one of the constraints that faces WPT, the low range. The other form of the WPT is the inductive platforms that wirelessly transmit the power to a device inside an experimental apparatus or a home cage. This technique suffers from a lower operational distance than far-field RF communication. The wireless head-mountable device in ref [36], for instance, receives the peak magnetic field when it is at the height of 0.5 to 2 cm above the induction platform, with a reduction of 30% at 3 cm [76]. The operational distance is a function of the transmitted power; the power level must be substantially smaller than the maximum permissible exposure limits (3.03 mW/cm^2) for humans in controlled environment [15], and 1.6W/Kg for specific absorption rate (SAR) averaged over 1 g of tissue [69, 77, 78]. On the other side, despite the need to be periodically replaced or recharged, batteries are a reliable approach to deliver a relatively high-power for a wide volume light delivery system, with a small-enough headstage as in the case of our work. In general, batteries are preferred for behavior experiments over animals that may need a further communication range such as songbirds [79], flying bats [80], rats [81], mice [37], cats [82] and monkeys [83-85]. Here, batteries represent 60% of the total weight of our system. This leaves a room for improvement by working on enhancing the coupling efficiency between the TF and LD, which will directly

help in lowering the power consumption and consequently the total size and weight. The size of the headstage (14.0 x 13.5 mm^2) is comparable with the size of other systems proposed in the literature (see the detailed comparison in **Table III**) and, as shown by the dimensions in **Fig8**. It fits in the size of the skull of adult (60 postnatal days) male C57BL/6J mice (width: 11.5 mm, ventral length: 17.0 mm, dorsal length: 22.0 mm for a 60 postnatal days male C57BL/6J [86]). Replacing batteries with a WPT system may help in reducing the total weight; however, it may shorten the wireless range as well as the pulse width of the generated pulses.

D. Wireless communication

The stimulation parameters (frequency, duty cycle, and pulse duration) are transmitted to the headstage wirelessly by infrared at $\lambda \sim 950$ nm; the output power of the LD is regulated manually by the trimmer. The tiny size and the low mass of the IR receiver help in building a miniaturized headstage since the receiver is a single component. Moreover, the IR communication has the advantage of offering a reliable communication without interference with nearby radio frequency (RF) signals. The battery-powered IR wireless headstage is a versatile, flexible setup that can be adapted to different environments from a home cage to a freestyle maze; since the number of IR LEDs can be increased to cover any blind spot in the arena. IR is an inexpensive and easy technique for wireless communication that is widely used for short-range (1-5 m) communication [35, 37, 39, 87, 88]. IR light is very similar to visible light, except that it has a slightly longer wavelength, typically in the range of 940-950 nm. This means IR is invisible to partially blind rats and mice with dichromatic vision [89] that creates a convenient wireless communication technique for free behavior readout experiments. IR communication is limited to line of sight whereas RF communication can achieve a higher range of communication and data rate without line of sight (see **Table V**). For wireless implantable devices RF communication is preferable for bi-directional communication. It requires taking into consideration RF signal orientation and polarization; therefore a careful antenna design is required [87]. There is an arising new networking technology called light fidelity Li-Fi [90-92], which may limit the domination of RF communication, since it claims that it is 100 times faster than the traditional Wi-Fi and can offer a bi-directional communication. In future work, the principle of communication between the transmitter and the head-mountable device can be integrated to a Li-Fi setup for mice *in vivo* arena for high data rate transmission.

VII. CONCLUSION

The system presented in this work exploits the unconventional coupling of a semiconductor LD to TF on a wireless-driven platform to obtain wide-volume illumination in deep-brain regions, an approach so far limited to optogenetic tethering stimulation techniques. The system has a low total cost since it employs a cost-effective LD and commercially available components. Moreover, setting up the coupling between a semiconductor LD and TF on a self-consistent wireless platform opens the door for more complex light delivery modulation along the taper segment.

APPENDIX

To estimate the light power density (intensity, p) around the TF for a given total output power, at a certain coupling position, we use the system depicted in **Fig S1**. Under the assumption of a perfectly axially symmetrical light power distribution, $p(r, \emptyset, z)$, around the taper, and by using the intensity profile extracted from the light emission of TF in a PBS:fluorescein solution (e.g. **Fig5 (a)**), p can be estimated. The total output power radiated from the taper surface P can be expressed as:

$$P = \int p(r, \emptyset, z) \, d\Sigma, \qquad (1)$$

Where Σ represents the taper surface. Considering that p is assumed to be constant with respect to $\emptyset$, $r = z \tan(\psi/2)$ on the taper surface, and

$$d\Sigma = 2\pi z \tan\frac{\psi}{2} \left[\cos\frac{\psi}{2}\right]^{-1} dz, \qquad (2)$$

It follows

$$P = 2\pi \tan\frac{\psi}{2} \left[\cos\frac{\psi}{2}\right]^{-1} \int_0^L z \, p(z) dz. \qquad (3)$$

Since the integral in (3) can be numerically estimated starting from the normalized experimental profile, $P_{norm}(z)$, with exception for a multiplicative constant, the estimation of the power density distribution along one arbitrary ruling of the conical surface can be obtained as

$$p(z) = \frac{P}{2\pi} \left[\int_0^{L'} z \, P_{norm}(z) \, dz\right]^{-1} \cos\frac{\psi}{2} \left[tan\frac{\psi}{2}\right]^{-1} P_{norm}(z).$$

$$(4)$$

L', represents the length of the line along the TF, where the intensity profile is collected (e.g. the cyan line in the bright field image in **Fig5 (a)**. **Fig5 (b)** shows the result of such estimation for 0.39 NA TF ($\Psi \sim 4°$, L$\sim$2.7 $\mp$ 0.1 mm), at coupling position #4, for a given total output power $P = 1.7$ mW. **Fig.S2** shows another example of power distribution around the tapered segment of a TF with a lower angle ($\Psi \sim 3°$, L$\sim$3.2 $\mp$ 0.1 mm). TFs with low taper angle distributes the power uniformly over larger surface with a lower power density near the tip.

REFERENCES

1.   Deisseroth, K., *Optogenetics*. Nat Meth, 2011. **8**(1): p. 26-29.

2. Pisanello, M., et al. *Photonic technologies for optogenetics*. in *Transparent Optical Networks (ICTON), 2014 16th International Conference on*. 2014.

3. Adamantidis, A.R., et al., *Neural substrates of awakening probed with optogenetic control of hypocretin neurons.* Nature, 2007. **450**(7168): p. 420-4.

4. Lobo, M.K., et al., *Cell Type Specific Loss of BDNF Signaling Mimics Optogenetic Control of Cocaine Reward.* Science (New York, N.Y.), 2010. **330**(6002): p. 385-390.

5. Packer, A.M., B. Roska, and M. Hausser, *Targeting neurons and photons for optogenetics.* Nat Neurosci, 2013. **16**(7): p. 805-815.

6. Boyden, E.S., et al., *Millisecond-timescale, genetically targeted optical control of neural activity.* Nat Neurosci, 2005. **8**(9): p. 1263-1268.

7. Yizhar, O., et al., *Optogenetics in neural systems.* Neuron, 2011. **71**(1): p. 9-34.

8. Sileo, L., et al. *Optical fiber technologies for in-vivo light delivery and optogenetics*. in *Transparent Optical Networks (ICTON), 2015 17th International Conference on*. 2015.

9. Segev, E., et al., *Patterned photostimulation via visible-wavelength photonic probes for deep brain optogenetics.* Neurophotonics, 2016. **4**(1): p. 011002-011002.

10. Pisanello, F., L. Sileo, and M. De Vittorio, *Micro- and Nanotechnologies for Optical Neural Interfaces.* Frontiers in Neuroscience, 2016. **10**(70).

11. McAlinden, N., et al., *Thermal and optical characterization of micro-LED probes for in vivo optogenetic neural stimulation.* Optics Letters, 2013. **38**(6): p. 992-994.

12. McCall, J.G., et al., *Fabrication and application of flexible, multimodal light-emitting devices for wireless optogenetics.* Nat. Protocols, 2013. **8**(12): p. 2413-2428.

13. McAlinden, N., et al., *Optogenetic activation of neocortical neurons in vivo with a sapphire-based micro-scale LED probe.* Front Neural Circuits, 2015. **9**: p. 25.

14. Scharf, R., et al., *Depth-specific optogenetic control in vivo with a scalable, high-density μLED neural probe.* Scientific Reports, 2016. **6**: p. 28381.

15. Kim, T.I., et al., *Injectable, cellular-scale optoelectronics with applications for wireless optogenetics.* Science, 2013. **340**(6129): p. 211-6.

16. Ayub, S., et al., *An Intracerebral Probe with Integrated 10×1μLED Array for Optogenetic Experiments at 460 nm.* Procedia Engineering, 2015. **120**: p. 472-475.

17. Ayub, S., et al. *High-density probe with integrated thin-film micro light emitting diodes (μLEDs) for optogenetic applications*. in *2016 IEEE 29th International Conference on Micro Electro Mechanical Systems (MEMS)*. 2016.

18. Wu, F., et al., *Monolithically Integrated μLEDs on Silicon Neural Probes for High-Resolution Optogenetic Studies in Behaving Animals.* Neuron, 2015. **88**(6): p. 1136-1148.

19. Zorzos, A.N., E.S. Boyden, and C.G. Fonstad, *Multiwaveguide implantable probe for light delivery to sets of distributed brain targets.* Optics Letters, 2010. **35**(24): p. 4133-4135.

20. Zorzos, A.N., et al., *3-Dimensional Multiwaveguide Probe Array for Light Delivery to Distributed Brain Circuits.* Optics letters, 2012. **37**(23): p. 4841-4843.

21. Pisanello, F., et al., *Multipoint-emitting optical fibers for spatially addressable in vivo optogenetics.* Neuron, 2014. **82**(6): p. 1245-54.

22. Pisanello, M., et al., *Modal demultiplexing properties of tapered and nanostructured optical fibers for in vivo optogenetic control of neural activity.* Biomedical Optics Express, 2015. **6**(10): p. 4014.

23. Acker, L., et al., *FEF inactivation with improved optogenetic methods.* Proceedings of the National Academy of Sciences, 2016. **113**(46): p. E7297-E7306.

24. Park, S., et al., *One-step optogenetics with multifunctional flexible polymer fibers.* Nat Neurosci, 2017. **advance online publication**.

25. Pisanello, F., et al., *Dynamic illumination of spatially restricted or large brain volumes via a single tapered optical fiber.* Nat Neurosci, 2017. **advance online publication**.

26. Lu, C., et al., *Flexible and stretchable nanowire-coated fibers for optoelectronic probing of spinal cord circuits.* Science Advances, 2017. **3**(3).

27. Ki Yong, K., et al. *Integrated slanted microneedle-LED array for optogenetics*. in *Engineering in Medicine and Biology Society (EMBC), 2013 35th Annual International Conference of the IEEE*. 2013.

28. Kwon, K.Y., et al. *Head-mounted LED for optogenetic experiments of freely-behaving animal*. 2016.

29. Park, S.I., et al., *Soft, stretchable, fully implantable miniaturized optoelectronic systems for wireless optogenetics.* Nat Biotech, 2015. **33**(12): p. 1280-1286.

30. Montgomery, K.L., et al., *Wirelessly powered, fully internal optogenetics for brain, spinal and peripheral circuits in mice.* Nat Meth, 2015. **12**(10): p. 969-974.

31. Yeh, A.J., et al., *Wirelessly powering miniature implants for optogenetic stimulation.* Applied Physics Letters, 2013. **103**(16): p. 163701.

32. Shin, G., et al., *Flexible Near-Field Wireless Optoelectronics as Subdermal Implants for Broad Applications in Optogenetics.* Neuron, 2017. **93**(3): p. 509-521.e3.

33. Noh, K.N., et al., *Miniaturized, Battery-Free Optofluidic Systems with Potential for Wireless Pharmacology and Optogenetics.* Small, 2018. **14**(4): p. 1702479-n/a.

34. Park, S.I., et al., *Stretchable multichannel antennas in soft wireless optoelectronic implants for optogenetics.* Proceedings of the National Academy of Sciences, 2016. **113**(50): p. E8169-E8177.

35. Iwai, Y., et al., *A simple head-mountable LED device for chronic stimulation of optogenetic molecules in freely moving mice.* Neurosci Res, 2011. **70**(1): p. 124-7.

36. Wentz, C.T., et al., *A wirelessly powered and controlled device for optical neural control of freely-behaving animals.* Journal of Neural Engineering, 2011. **8**(4): p. 046021.

37. Hashimoto, M., et al., *Programmable wireless light-emitting diode stimulator for chronic stimulation of optogenetic molecules in freely moving mice.* Neurophotonics, 2014. **1**(1): p. 011002.

38. Yuan, M., et al. *A wirelessly controlled optical stimulator for optogenetics application*. in *2015 IET International Conference on Biomedical Image and Signal Processing (ICBISP 2015)*. 2015.

39. Jeong, J.-W., et al., *Wireless Optofluidic Systems for Programmable In Vivo Pharmacology and Optogenetics.* Cell, 2015. **162**(3): p. 662-674.

40. Rossi, M.A., et al., *A wirelessly controlled implantable LED system for deep brain optogenetic stimulation.* Frontiers in Integrative Neuroscience, 2015. **9**: p. 8.

41. Sung Il, P., et al., *Ultraminiaturized photovoltaic and radio frequency powered optoelectronic systems for wireless optogenetics.* Journal of Neural Engineering, 2015. **12**(5): p. 056002.

42. McCall, J.G., et al., *Preparation and implementation of optofluidic neural probes for in vivo wireless pharmacology and optogenetics.* Nature Protocols, 2017. **12**: p. 219.

43. Lu, L., et al., *Wireless optoelectronic photometers for monitoring neuronal dynamics in the deep brain.* Proceedings of the National Academy of Sciences, 2018. **115**(7): p. E1374-E1383.

44. Ameli, R., et al. *A wireless and batteryless neural headstage with optical stimulation and electrophysiological recording*. in *2013 35th Annual International Conference of the IEEE Engineering in Medicine and Biology Society (EMBC)*. 2013.

45. Gagnon-Turcotte, G., et al., *A Wireless Optogenetic Headstage with Multichannel Electrophysiological Recording Capability.* Sensors, 2015. **15**(9): p. 22776.

46. Dagnew, R., et al. *CerebraLux: a low-cost, open-source, wireless probe for optogenetic stimulation*. 2017. SPIE.

47. Gagnon-Turcotte, G., et al., *A Wireless Headstage for Combined Optogenetics and Multichannel Electrophysiological Recording.* IEEE Transactions on Biomedical Circuits and Systems, 2017. **11**(1): p. 1-14.

48. Lee, S.T., et al., *A Miniature, Fiber-Coupled, Wireless, Deep-Brain Optogenetic Stimulator.* IEEE Transactions on Neural Systems and Rehabilitation Engineering, 2015. **23**(4): p. 655-664.

49. Maghsoudloo, E., et al. *A Smart Neuroscience Platform with Wireless Power Transmission for Simultaneous Optogenetics and Electrophysiological Recording*. in *2018 IEEE International Symposium on Circuits and Systems (ISCAS)*. 2018.

50. Kwon, K.Y., et al. *A wireless slanted optrode array with integrated micro leds for optogenetics*. in *2014 IEEE 27th International Conference on Micro Electro Mechanical Systems (MEMS)*. 2014.

51. Lee, H.M., et al. *A wireless implantable switched-capacitor based optogenetic stimulating system*. in *2014 36th Annual International*

This article has been accepted for publication in a future issue of this journal, but has not been fully edited. Content may change prior to final publication. Citation information: DOI 10.1109/TBME.2018.2882146, IEEE Transactions on Biomedical Engineering

TBME-01112-2018.R1

8

Conference of the IEEE Engineering in Medicine and Biology Society. 2014.

52. Kwon, K.Y., et al., *Design, fabrication, and packaging of an integrated, wirelessly-powered optrode array for optogenetics application.* Front Syst Neurosci, 2015. **9**: p. 69.

53. Schwaerzle, M., et al. *Miniaturized tool for optogenetics based on an LED and an optical fiber interfaced by a silicon housing.* in *2014 36th Annual International Conference of the IEEE Engineering in Medicine and Biology Society.* 2014.

54. Bi, X., et al., *A Flexible, Micro-Lens-Coupled LED Stimulator for Optical Neuromodulation.* IEEE Transactions on Biomedical Circuits and Systems, 2016. **PP**(99): p. 1-7.

55. Stark, E., T. Koos, and G. Buzsaki, *Diode probes for spatiotemporal optical control of multiple neurons in freely moving animals.* J Neurophysiol, 2012. **108**(1): p. 349-63.

56. Cao, H., et al., *An Integrated μLED Optrode for Optogenetic Stimulation and Electrical Recording.* IEEE Transactions on Biomedical Engineering, 2013. **60**(1): p. 225-229.

57. Li, Y., et al., *Thermal analysis of injectable, cellular-scale optoelectronics with pulsed power.* Proceedings of the Royal Society A: Mathematical, Physical and Engineering Science, 2013. **469**(2157).

58. Gagnon-Turcotte, G., et al. *A wireless photostimulator for optogenetics with live animals.* in *2017 15th IEEE International New Circuits and Systems Conference (NEWCAS).* 2017.

59. Bi, X., B. Fan, and W. Li. *Micro-lens-coupled LED neural stimulator for optogenetics.* in *2015 IEEE Biomedical Circuits and Systems Conference (BioCAS).* 2015.

60. *Blue Laser Diode in TO38 ICut PAckage (PL 450B, OSRAM) (2017, August 04). Retrieved from https://www.osram-os.com/Graphics/XPic1/00246126_0.pdf/PL%20450B.pdf.* 2015.

61. Leifer, A.M., et al., *Optogenetic manipulation of neural activity in freely moving Caenorhabditis elegans.* Nat Meth, 2011. **8**(2): p. 147-152.

62. Bruegmann, T., et al., *Optogenetic control of contractile function in skeletal muscle.* Nat Commun, 2015. **6**: p. 7153.

63. Taslimi, A., et al., *An optimized optogenetic clustering tool for probing protein interaction and function.* Nat Commun, 2014. **5**: p. 4925.

64. Alexander, M.A., et al., *An optical neural interface: in vivo control of rodent motor cortex with integrated fiberoptic and optogenetic technology.* Journal of Neural Engineering, 2007. **4**(3): p. S143.

65. Fan, F., et al., *A monolithic white laser.* Nat Nanotechnol, 2015. **10**(9): p. 796-803.

66. Rossi, M.A., N. Calakos, and H.H. Yin, *Spotlight on movement disorders: What optogenetics has to offer.* Mov Disord, 2015. **30**(5): p. 624-31.

67. Childs, C., *Human brain temperature: regulation, measurement and relationship with cerebral trauma: Part 1.* British Journal of Neurosurgery, 2008. **22**(4): p. 486-496.

68. Andersen, P. and E.I. Moser, *Brain temperature and hippocampal function.* Hippocampus, 1995. **5**(6): p. 491-498.

69. Aldaoud, A., et al., *Wireless multichannel optogenetic stimulators enabled by narrow bandwidth resonant tank circuits.* Sensors and Actuators A: Physical, 2018. **271**: p. 201-211.

70. Gagnon, L.L., et al. *A wireless system for combined heart optogenetics and electrocardiography recording.* in *2017 IEEE International Symposium on Circuits and Systems (ISCAS).* 2017.

71. Gagnon-Turcotte, G., et al. *Wireless brain computer interfaces enabling synchronized optogenetics and electrophysiology.* in *2017 IEEE International Symposium on Circuits and Systems (ISCAS).* 2017.

72. Ahire, D.B. and V.J. Gond. *Wireless power transfer system for biomedical application: A review.* in *2017 International Conference on Trends in Electronics and Informatics (ICEI).* 2017.

73. Chang, C.-W. and J.-C. Chiou, *A Wireless and Batteryless Microsystem with Implantable Grid Electrode/3-Dimensional Probe Array for ECoG and Extracellular Neural Recording in Rats.* Sensors, 2013. **13**(4): p. 4624.

74. Merli, F., et al., *Design, Realization and Measurements of a Miniature Antenna for Implantable Wireless Communication Systems.* IEEE Transactions on Antennas and Propagation, 2011. **59**(10): p. 3544-3555.

75. Gutruf, P. and J.A. Rogers, *Implantable, wireless device platforms for neuroscience research.* Current Opinion in Neurobiology, 2018. **50**: p. 42-49.

76. Warden, M.R., J.A. Cardin, and K. Deisseroth, *Optical Neural Interfaces.* Annual review of biomedical engineering, 2014. **16**: p. 103-129.

77. Hsing-Yi, C. and W. Hou-Hwa, *Current and SAR induced in a human head model by the electromagnetic fields irradiated from a cellular phone.* IEEE Transactions on Microwave Theory and Techniques, 1994. **42**(12): p. 2249-2254.

78. *IEEE Standard for Safety Levels With Respect to Human Exposure to Radio Frequency Electromagnetic Fields, 3 kHz to 300 GHz.* IEEE Std C95.1-1991, 1992: p. 1.

79. Arfin, S.K., et al., *Wireless Neural Stimulation in Freely Behaving Small Animals.* Journal of Neurophysiology, 2009. **102**(1): p. 598-605.

80. Lancaster, W.C., O.W. Henson, and A.W. Keating, *Respiratory muscle activity in relation to vocalization in flying bats.* The Journal of Experimental Biology, 1995. **198**(1): p. 175-191.

81. Su, K., et al., *A wearable wireless system for olfactory neural recording in freely moving rats based on Wi-Fi technology.* Sensors and Actuators B: Chemical, 2015. **213**(Supplement C): p. 457-464.

82. Sherk, H. and E.J. Wilkinson, *A novel system for recording from single neurons in unrestrained animals.* Journal of Neuroscience Methods, 2008. **173**(2): p. 201-207.

83. Miranda, H., et al. *A high-rate long-range wireless transmission system for multichannel neural recording applications.* in *2009 IEEE International Symposium on Circuits and Systems.* 2009.

84. Mavoori, J., et al., *An autonomous implantable computer for neural recording and stimulation in unrestrained primates.* Journal of Neuroscience Methods, 2005. **148**(1): p. 71-77.

85. Lei, Y., et al., *Telemetric recordings of single neuron activity and visual scenes in monkeys walking in an open field.* Journal of Neuroscience Methods, 2004. **135**(1): p. 35-41.

86. Maga, A.M., *Postnatal Development of the Craniofacial Skeleton in Male C57BL/6J Mice.* Journal of the American Association for Laboratory Animal Science : JAALAS, 2016. **55**(2): p. 131-136.

87. McCall, J.G. and J.-W. Jeong, *Minimally invasive probes for programmed microfluidic delivery of molecules in vivo.* Current Opinion in Pharmacology, 2017. **36**: p. 78-85.

88. Sim, J.Y., et al., *Microfluidic neural probes: in vivo tools for advancing neuroscience.* Lab on a Chip, 2017. **17**(8): p. 1406-1435.

89. Jacobs, G.H., J.A. Fenwick, and G.A. Williams, *Cone-based vision of rats for ultraviolet and visible lights.* Journal of Experimental Biology, 2001. **204**(14): p. 2439-2446.

90. Vijayalakshmi, A. and N. Sudha. *New strategy in wireless communication: Li-Fi for delivery of broadband and media content in aircraft without intrusion.* in *2017 International Conference on Wireless Communications, Signal Processing and Networking (WiSPNET).* 2017.

91. Sahrawat, P.K. *Li-Fi: Future of Wireless Communication.* in *National Conference on Innovative Trends in Computer Science Engineering (ITCSE-2015).* 2015.

92. Haas, H. *High-speed wireless networking using visible light.* SPIE, 2013.

93. Hassan, S.M., et al., *Application of Wireless Technology for Control: A WirelessHART Perspective.* Procedia Computer Science, 2017. **105**: p. 240-247.

94. Abinayaa, V. and A. Jayan, *Case Study on Comparison of Wireless TEchnologies in Industrial Applications.* International Journal of Scientific and Research Publications, 2014. **4**(2).

95. Zatout, Y. *Using wireless technologies for healthcare monitoring at home: A survey.* in *2012 IEEE 14th International Conference on e-Health Networking, Applications and Services (Healthcom).* 2012.

96. Comission, F.C., *Human Exposure to Radiofrequency Electromagnetic Fields* 2013.

97. Kim, D.-H., et al., *Epidermal Electronics.* Science, 2011. **333**(6044): p. 838-843.

98. Jang, K.-I., et al., *Rugged and breathable forms of stretchable electronics with adherent composite substrates for transcutaneous monitoring.* Nature Communications, 2014. **5**: p. 4779.

99. Xu, S., et al., *Soft Microfluidic Assemblies of Sensors, Circuits, and Radios for the Skin.* Science, 2014. **344**(6179): p. 70-74.

100. Cecil, S., et al. *Numerical Assessment of Specific Absorption Rate in the Human Body Caused by NFC Devices*. in *2010 Second International Workshop on Near Field Communication*. 2010.

101. Fan, D., et al., *A Wireless Multi-Channel Recording System for Freely Behaving Mice and Rats*. PLoS ONE, 2011. **6**(7): p. e22033.

102. Szuts, T.A., et al., *A wireless multi-channel neural amplifier for freely moving animals*. Nat Neurosci, 2011. **14**(2): p. 263-9.

103. Hampson, R.E., V. Collins, and S.A. Deadwyler, *A wireless recording system that utilizes Bluetooth technology to transmit neural activity in freely moving animals*. Journal of Neuroscience Methods, 2009. **182**(2): p. 195-204.

104. Obeid, I., M.A.L. Nicolelis, and P.D. Wolf, *A multichannel telemetry system for single unit neural recordings*. Journal of Neuroscience Methods, 2004. **133**(1): p. 33-38.
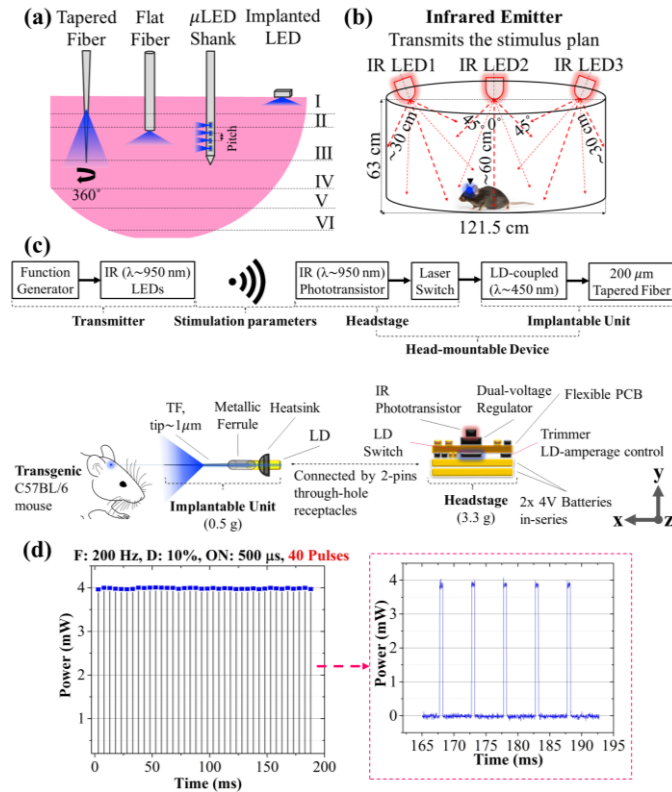
Fig. 1. System overview

(a) Schematic comparison between the different capabilities for each light delivery system. The implantable LEDs are ideal for stimulating the superficial cortical layers whereas the other systems are for deeper regions. However, TF are ideal for deeper regions since they are minimal invasive and offers a large illuminated volume. **(b)** Sketch of the proposed wireless optogenetic system. The IR emitter sends the stimulus parameters to a head-mountable device fixed on the head of a transgenic mouse. **(c)** System block diagram and data flow from the function generator until it reaches the implantable TF. **(d)** 4 mW output power pulses emitted by the head-mountable device at TTL trigger signal (F: 200 Hz, D: 10%, Pulse-width: 500μs).
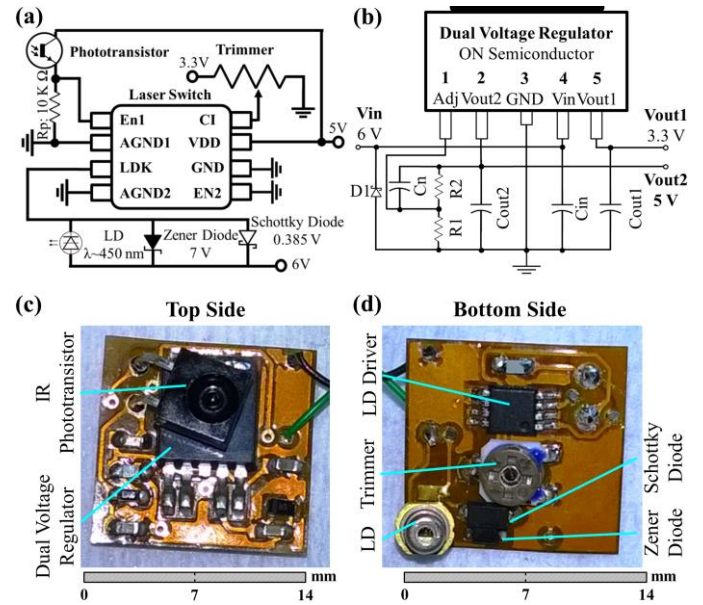

Fig. 2. Headstage circuit diagram

(a) Circuit diagram of the laser driving circuit on the headstage (top-copper), which comprises the laser diode switch, the output optical power tuning trimmer, the laser diode protection circuit, and the receptacles for connecting the headstage to the implantable unit. **(b)** Circuit diagram of the power module on the headstage (bottom-copper), which compromises the dual voltage regulator, the IR phototransistor receiver, and the battery terminals. **(c-d)** Two photographs of top and bottom sides of the headstage after hand-soldering all the components.
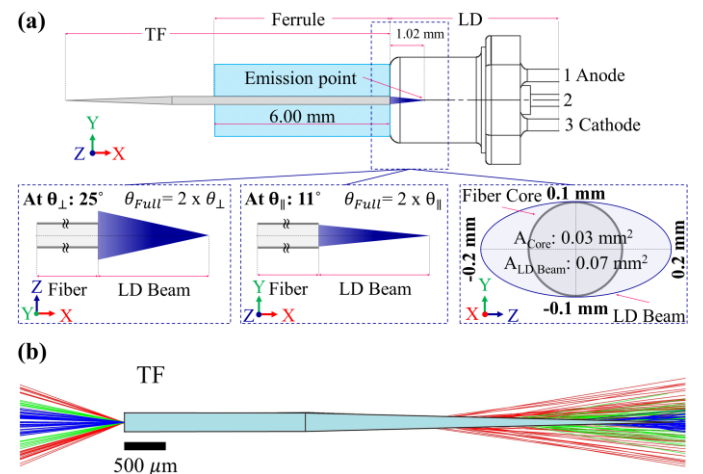

Fig. 3. Headstage circuit diagram

(a) Schematic side view of the coupling between the LD and TF connectorized to a corresponding metallic ferrule. Below are the launching conditions between the LD beam (maximum divergence angles at FWHM, $\theta_\perp \times \theta_{//}$: 25°x11°) and TF core (Ø200 μm). **(b)** Ray tracing schematic of the implantable 0.39 NA tapered fiber. Red, green, and blue rays at high, low, and almost at the center injected angles to the fiber facet respectively. Rays with higher injected angles are out-coupled further from the tip: the higher the injected angle, the further out-coupled ray from the tip.
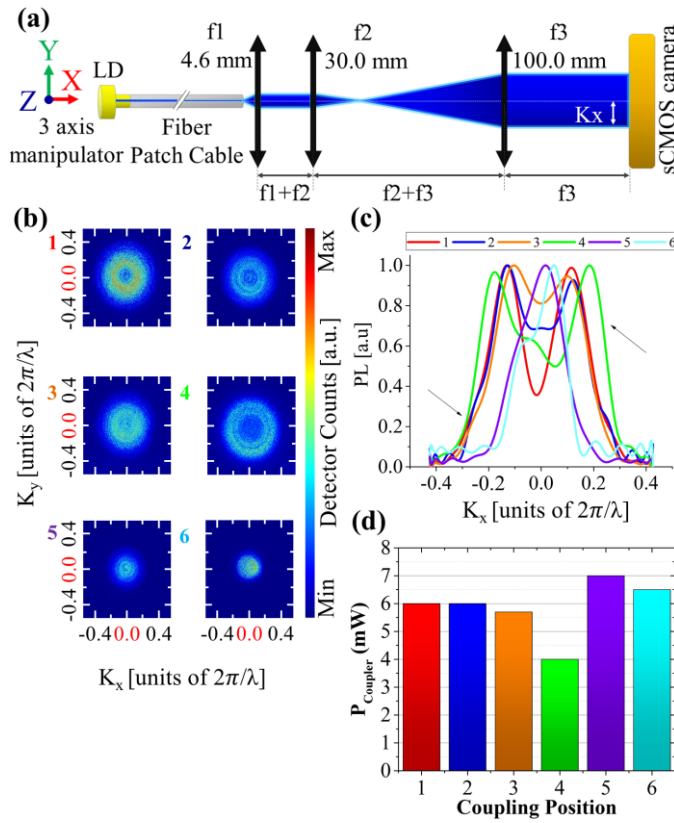
Fig. 4. The optical properties of the coupler

(a) Schematic of the optical setup for collecting far fields images of the fiber end facet by sCMOS camera. The laser diode (LD) is set on 3-axis micromanipulator and coupled to a fixed 0.39 NA optical fiber patch cable (200/225 μm). The movement of the LD over the 3-axis micromanipulator in respect to the fixed optical fiber changes coupling position and therefore changes the injected guided modes into the fiber. (b) Far field images of the fiber output end facet at six different coupling positions with respect to the wave vector axis K_Y & K_X. (c) Superposition of the six coupling positions with respect to the K_x axis. The graph of each coupling position is identified by a different color to facilitate the comparison between the different coupling positions according to the output power and the width with respect to the wave-vector values. The coupling position # 4 is the widest along the K_x axis. (d) Total collected output optical power ($P_{Coupling}$) for each coupling position with the corresponding number and color. The highest measured power level was at coupling position no. 5.
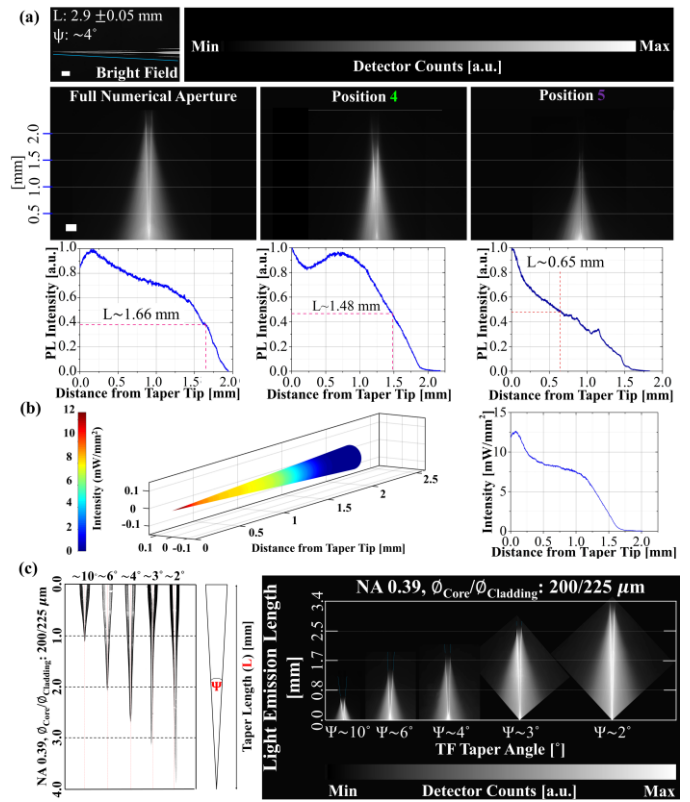

Fig. 5. The achieved light emission out of the coupler

(a) Light emission out of TF with taper angle $\Psi \sim 4°$ at three different coupling positions. Full Numerical Aperture position (far left), obtained by using table top optical mounts, resulting emission length is L$\sim$ 1.66 mm. Coupling position no. 4 achieves L$\sim$1.48 mm light emission length. Coupling position no. 5 achieves L$\sim$0.65 mm light emission length. All the profiles were collected along the cyan line in the bright field image. Scale bar is 200 μm. (b) The power density along and around the TF ($\Psi \sim 4°$, L$\sim$2.7 $\pm$ 0.1 mm) at coupling position no. 4. (c) Left, a group of TFs with different taper angles ($\Psi \sim$10 to 2°). Right, the same group of tapers coupled at position no. 4 then submerged in a droplet of PBS:fluorescein solution to the show the regulation of the emission length with respect to the taper length and angle.
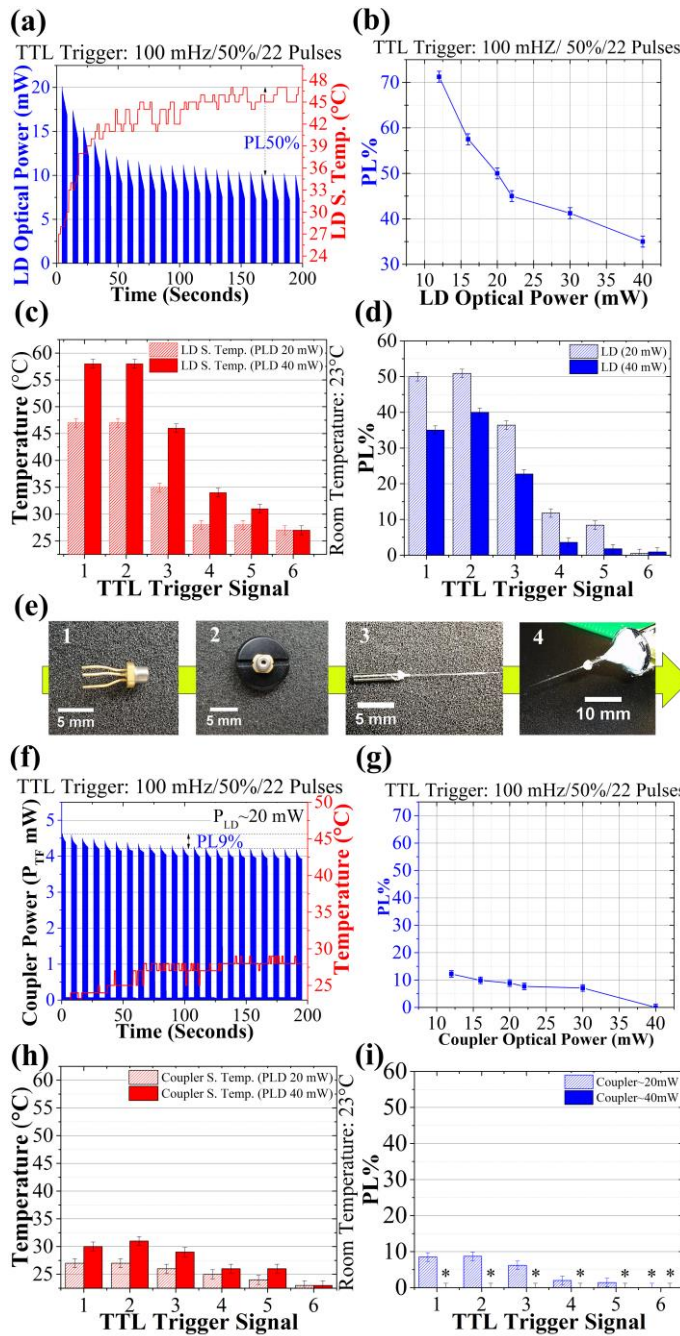
Fig. 6. The implantable unit thermal properties

(a) Typical example of output optical power (P_{LD}) and temperature of a bare laser diode cane (T_{Case}) along 3 minutes of continuous operation at TTL trigger signal: 100 mHz/ 50%/22-Pulses (5s on & 5s off). (b) Power loss percentage (PL%) at six different output optical power (P_{LD}) levels at the end of 3 minutes of continuous operation at TTL trigger signal: 100 mHz/50%/22-Pulses (5s on & 5s off). (c-d) T_{case} and PL% for 3 minutes of continuous operation of a bare LD at P_{LD}~40 mW and P_{LD}~20 mW at six different TTL Trigger Signal: (1) 100 mHz/50%, (2) 333 mHz/50%, (3) 40 Hz/40%, (4) 10 Hz/25%, (5) 20 Hz/20%, (6) 30 Hz/15%. (e) The preparation of the implantable unit from a bare LED at (1) to a complete unit at (4). (f) Output optical power of the coupler (P_{TF}), along with the surface temperature of the coupler, at P_{LD}~20 mW. (g) Power loss percentage (PL%), after the realization of the coupling as represented in panel e4. (h-i) Graphs exhibit the temperature of the diode laser case (T_{case}) and PL% for 3 minutes of continuous operation after enhancing the heat dissipation, for the same TTL trigger signals of panels (c-d). Panels (a-d) can go in a direct comparison with panels (f-i) to show the difference in the optical and thermal characteristics before and after building a coupler.
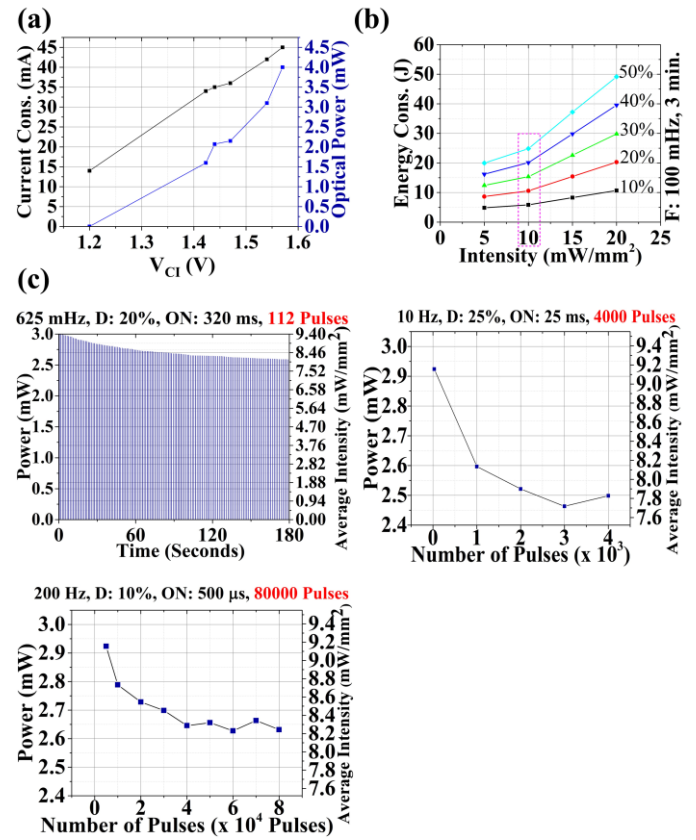

Fig. 7. Power consumption

(a) Relationship between the total current consumption of the headstage and the P_{TF} (the emitted power at the TF tip) at different values of the regulating V_{CI} of the laser switch. (b) The energy consumption (J) at the end of 3 minutes of continuous operation for different optical power intensities at different TTL trigger signal with different duty cycles (D). (c) Left-top graph shows P_{TF} and the average power intensity along 3 minutes of continuous operation at TTL trigger signal 625mHz/20%/320ms. Right-top graph shows the P_{TF} and the average intensity at TTL 10Hz/25%/25ms along 4000 pulses, each blue dot represents the average of P_{TF} and intensity after multiple 1000 pulses of 75 ms. Left-down shows the same parameters at TTL 200Hz/10%/500μs along 80,000 pulses, each blue dot represents the average of P_{TF} and intensity after multiple 10,000. In all the three figures, the head-mountable device was powered by two 3.7V/50mAh lithium polymer rechargeable batteries (GM051215, PowerStream).
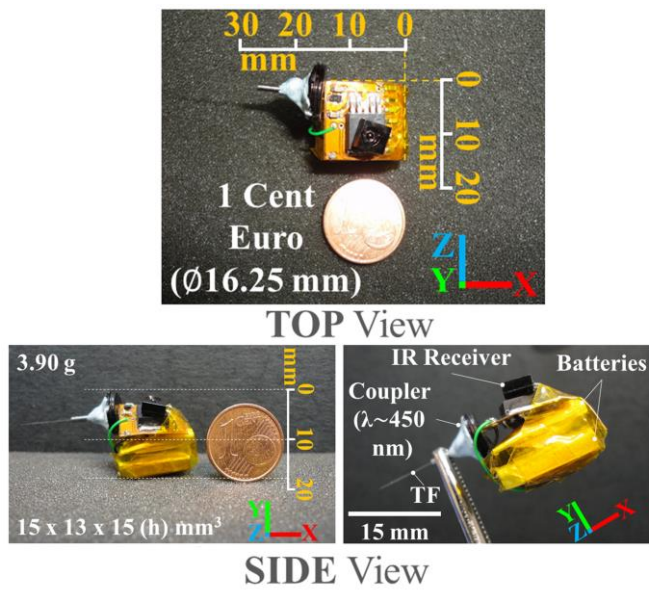
Fig. 8. The head-mountable device. Photos of different views of the complete head-mountable device.
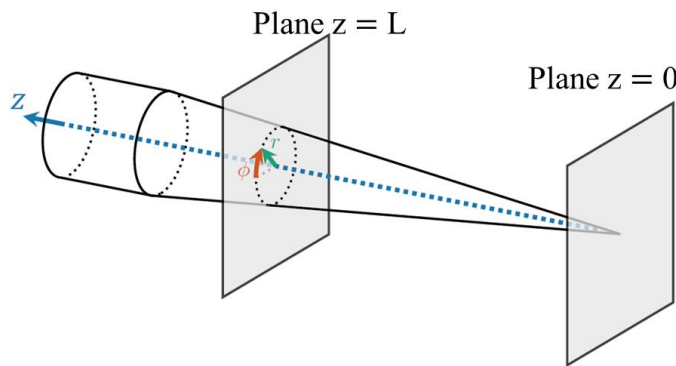

Fig. S1. Cylindrical coordinate system adopted for the estimation of light power density.
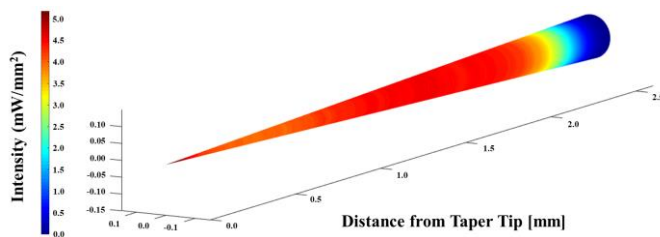

Fig. S2. The power density along and around the TF ($\Psi\sim3°$, L$\sim3.2 \pm 0.1$ mm) at coupling position no. 4.

Table1
The weight of the head-mountable device

Component	Weight (g)
Headstage	0.8
Coupler	0.5
Battery (#2)	2.5
Total	3.8

Table II System Characteristics	
Parameter	Value
Input Voltage	6 V
Current Consumption (LD OFF)	1 mA (LD_OFF)
Current Consumption (LD ON, 12.5 mW/mm^2)	45 mA (12.5 mW/mm^2)
Light Source	Semiconductor Laser Diode (OSRAM, Q65111A0518, λ~450 nm)
Implantable TF	0.39 NA TF (∅ 200/225 μm) The light emission length along the tapered segment can be tailored from ~400μm to ~3mm by acting on the taper angle (2°<Ψ<10°).
Wireless TTL Trigger Signal	IR, λ~950 nm
Power source	1. Two Batteries: 3 V, 225 mAh, Lithium Manganese Dioxide Coin Button Battery (CR2032)(non-rechargeable)(RS Pro, 866-0672), 20 x 3.2 mm, Weight (2 Batteries): 6.2 g 2. Two Batteries: 3 V, 140 mAh, Lithium Manganese Dioxide Coin Button Battery (CR2025) (non-rechargeable) (RS Pro, 866-0663), 20 x 2.5 mm, Weight (2 Batteries): 4.40 g 3. Two Batteries: 3.7 V, 50 mAh, Lithium ion Battery (rechargeable) (Powerstream, M041215), 15 x 12 x 5 mm, Weight (2 Batteries): 2.5 g
Head-mountable total weight according to the used batteries	1. 7.5 g 2. 5.7 g 3. 3.8 g
Battery life time at 10 mW/mm^2 and 25% duty cycle	1. Expected: 20 hours (non-stop operation) 2. Expected:12 hours (non-stop operation) 3. Expected: 4 hours (non-stop operation)

Table III Comparison of wireless head-mountable devices

Device	Size	Weight	Power source; running time	Light source	Implantable part	Wireless control	Light source amperage control	Validated TTL Pulse width range	Main application
(Iwai et al. 2011) [35]	24 x9 x9 mm	3.1 g	2 x coin cells (3 V/30 mAh); 125 min @ D: 50%	7 mW LED (Ø 3mm)	LED (Ø 3mm)	Infrared (IR)	X (fixed resistor)	(300 μs to 300 ms)	Stimulating superficial cortical layers
Wentz et al. 2011) [36]	< 1 cm3	3 g	Wireless energy transfer-super capacitor ~7.5 cm	- LED (1 x 1 mm)	LED (1 x 1 mm)	RF	-	-	Stimulating superficial cortical layers. Social experiments to run several devices simultaneously
(Ameli et al. 2013) [44]	15 x25 x17 mm	7.4 g	Wireless energy transfer-super capacitor <7 cm	Flat fiber-coupled LED	FF	RF	✓ (wirelessly)	(100 μs to 2.25 s)	Stimulation (1 CH) and electrophysiological recording (2 microelectrodes)
(Hashimoto et al. 2014)[37]	14 x14 x10 mm	2.4 g	1 Rechargeable battery (3.7 V/10 mAh); <67min @ D:50%	6.07 mW/mm^2 LED (1.6 x0.8 x0.68 mm), 4.6 mW/mm^2 LED (1 x0.5 x0.5 mm)	LED (1.6 x0.8 x0.68 mm) or (1 x0.5 x0.5 mm)	IR	X (fixed resistor)	>1 ms	Stimulating superficial (3 CHs) cortical layers. Social experiments to run several devices
(Gagnon-Turcotte et al. 2017)[47]	17 x18 x10 mm	4.9 g	1 Battery (3.7V/100 mAh); 70 min @ D: 10%	(70 mW/mm^2; 2.19 mW) Optical flat fiber-coupled LED	FF (core 200μm)	RF	X (fixed resistor)	-	Stimulation (1 CH) and electrophysiological recording (8 microelectrodes)
(Dagnew et al. 2017)[46]	0.95 cm3	2.8 g	1 Rechargeable battery (3.7 V/ 20mAh) 35 min	(4.2 mW/mm^2; 825 μm) Optical flat fiber-coupled LED (450/500 μm)	FF (450/500 μm)	IR	✓ (wirelessly)	-	The presence of the optical fiber makes the device suitable for light delivery beyond the cortical layers
Proposed	15 x13 x15 mm	3.8 g	2 x Rechargeable batteries (3.7V/50mAh) 240 min @ D:25%	10 mW/mm^2 Tapered optical fiber-coupled LD	TF (Ø225/200 μm), tip~ <1 μm	IR	✓ (trimmer)	>20 μs	Deep brain stimulation with minimal invasiveness

Table IV Comparison of μLEDs based wireless optogenetic stimulation devices with our proposed system

	Array of	Max full emission length	Probe Thickness	Probe Width	Max optical power density (mW/mm²)/ Electrical input power (mW)	Weight	Power source	Mounting setup
[Kim et al., 2013] [15]	4 μ-ILEDs (6.45 μm thick, 50 x 50 μm²)	~200 μm	~20 μm	~400 μm	40/40	-	WPT	Head-mountable
[Jeong et al., 2015] [39]	4 μ-ILEDs (6.45 μm thick, 100 x 100 μm²)	~400 μm	~80 μm	~500 μm	-	~1.8 g	Battery	Head-mountable
[Rossi et al., 2015] [40]	2 μLEDs (140 μm thick, 240 x 320 μm²)	Two ~320 μm illuminated segments with a pitch of ~4 mm	~100 μm	~700 μm	30/32	2.9 g	Battery	Head-mountable
[Park et al., 2015] [41]	4 μ-ILEDs (100 x 100 μm²)	~400 μm	~10 μm	~250 μm	1/2	~70 mg	WPT	Head-mountable
[Shin et al., 2017] [32]	1 μ-ILEDs (50 μm thick, 270 x 220 μm²)	~220 μm	~80-130 μm	~350 μm	200/62	~30 mg	WPT	Fully implantable
[Noh et al., 2018] [33]	4 μ-ILEDs (50 μm thick, 270 x 220 μm²)	~880 μm	~80 μm	~500 μm	85/1000	220 mg	WPT	Fully implantable
Proposed	TF	~2 mm	TF, outer diameter < Ø225 μm to tip (~500 nm)		10/270	3.8 g	Battery	Head-mountable

Table V Overview of wireless data transfer and power transfer for implantable devices [75, 88, 93-96]

| | Wireless Data Communication | | | | Power Supply Options | | | |
| | | Radio Frequency (RF) (20 KHz – 300 GHz) | | | Electrochemical sources | Wireless power harvester | | |
	Infrared (IR)	Bluetooth (IEEE802.15.1)	Wi-Fi (IEEE802.11x)	Radio Communication (IEEE 802.15.4)	Battery powered	Solar + Far field	Near Field Inductive coupling	Far field energy
Frequency	Typically 38 KHz carrier	2.4 GHz	2.4-5.8 GHz	868/915 MHz or 2.4 GHz	-	-	13.56 MHz	1-2.7 GHz
Range	1-5 m	10 m	100 m	10 m	-	~< 20 cm	A few centimeters	~< 20 cm
Data rate	0.5-1 Kbps	Up to 1 Mbps	11-200 Mbps	250 Kbit/s	-	-	-	-
Data transfer	Uni-directional	Bi-directional	Bi-directional	Bi-directional	-	-	-	-
Applications	-Head-mountable LED device [35, 37] -Head-mountable (light delivery μLED + drug delivery) device [39] - Head-mountable Flat fiber-coupled LED [46]	-Wireless multi-channel recording Device [73, 103]	- Wireless multi-channel recording Device [81, 104]	- Head-mountable LED & μLED Devices [36, 38] -Head-mountable Flat fiber-coupled LED[44, 45, 47] - Head-mountable μ-ILED [15, 41] - Wireless multi-channel recording Device [101, 102]	-Head-mountable implantable LED & LED Shank device [35, 37, 40] - Head-mountable (light delivery μLED + drug delivery) device [39] - Head-mountable Flat fiber-coupled LED [45-47] - Wireless multi-channel recording Device [81, 101-103]	- Head-mountable μ-ILEDs Device [41]	-Head-mountable Flat fiber-coupled LED & recording [44] - Head-mountable μLED (light delivery & recording)[50] - Fully-implantable μ-ILED Device[32]	- Head-mountable μILED & LED shank Devices [15, 38, 40] - Fully-implantable LED & μLEDs Devices [29-31, 33, 34] - Head-mountable Flat fiber-coupled LED (light delivery & recording)[45, 47] - Epidermal Devices [97-99]
Setup	Line of sight	Transcutaneous	Transcutaneous	Transcutaneous	External	External	Transcutaneous	Transcutaneous
Electromagnetic impact	-	-	-	-	none	Medium (SAR~20 mW/Kg[41])	Low (SAR~11.18 mW/Kg)[100]	High (SAR 1100 [31]-69 [29] mW/Kg)